ACS OMEGA

Article

http://pubs.acs.org/journal/acsodf

Direct Realization of Complete Conversion and Agglomeration Dynamics of SnO_2 Nanoparticles in Liquid Electrolyte

Joon Ha Chang,[†,‡,§] Jun Young Cheong,[‡,§] Jong Min Yuk,[‡] Chanhoon Kim,[‡] Sung Joo Kim,[†,‡] Hyeon Kook Seo,[†,‡] Il-Doo Kim,[*,‡] and Jeong Yong Lee[*,†,‡]

[†]Center for Nanomaterials and Chemical Reactions, Institute for Basic Science (IBS), 1689 Yuseong Dae-ro 70, Daejeon 305-701, Republic of Korea

[‡]Department of Materials Science & Engineering, Korea Advanced Institute of Science & Technology, 335 Science Road, Daejeon 305-701, Republic of Korea

S *Supporting Information*

ABSTRACT: The conversion reaction is important in lithium-ion batteries because it governs the overall battery performance, such as initial Coulombic efficiency, capacity retention, and rate capability. Here, we have demonstrated in situ observation of the complete conversion reaction and agglomeration of nanoparticles (NPs) upon lithiation by using graphene liquid cell transmission electron microscopy. The observation reveals that the Sn NPs are nucleated from the surface of SnO_2, followed by merging with each other. We demonstrate that the agglomeration has a stepwise process, including rotation of a NP, formation of necks, and subsequent merging of individual NPs.

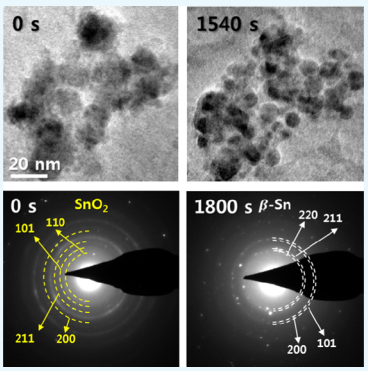

INTRODUCTION

The conversion reaction ($M^{z+}X_y + zLi^+ \leftrightarrow M + yLi_{z/y}X$, where M and X represent the cation and anion, respectively) is a ubiquitous lithiation phenomenon in electrode materials, including metal oxides, sulfides, fluorides, and nitrides.[1−3] The conversion process in these electrodes is pivotal as it affects the initial Coulombic efficiencies, cycle retention, and reversibility of batteries.[4,5] Recently, it has been proposed from the literature[6−8] that additional capacity can arise from the electrode materials that undergo the conversion reaction, which brings more potential for utilizing conversion reaction-based electrode materials, giving strong potential for application for practical rechargeable batteries. Along with the conversion reaction, the agglomeration of electrode materials is another important factor because it is a frequent phenomenon among nanoparticles (NPs) when used as electrodes.[9−13] Agglomeration of NPs occurs inevitably and leads to decreased surface areas and structural degradation, resulting in severe capacity fading.[4] Fundamental understanding of how the conversion reaction and agglomeration takes place on NPs is critical for providing new insights on the advanced electrode designs, but some challenges still remain for the direct observation of NPs under lithiation in commercial liquid electrolyte.

Recent development of in situ transmission electron microscopy (TEM) enables direct observation of morphological and phase transitions of nanostructured electrodes, which is suitable to analyze reaction mechanisms during lithiation.[14−17] Among these in situ TEM techniques, graphene liquid cell (GLC) TEM is a versatile tool to observe lithiation dynamics of various electrodes in liquid electrolyte while maintaining high resolution.[18,19] This technique enables not only dipping NPs of active materials into liquid electrolytes but also lithiation of electrodes with electrons for imaging.

Using GLC-TEM, here, we first demonstrate both conversion and agglomeration dynamics of SnO_2 NPs, one of the highly researched materials for a lithium-ion battery (LIB) anode.[18] From the comparison of in situ GLC-TEM of NPs, with ex situ TEM images taken from the electrode after electrochemical lithiation, we verified reliability of the GLC-TEM technique.

RESULTS AND DISCUSSION

Conversion Dynamics and Growth of Sn. A schematic illustration on how SnO_2 NPs are encapsulated inside the GLC upon e-beam irradiation and the elemental distribution inside the GLC are shown in Figure 1. For the electrolytes, solvent mixture of ethylene carbonates (EC) and diethyl carbonates (DEC) with a volume ratio of 3:7 in addition to 10 wt % of fluoroethylene carbonate (FEC) with 1.3 M lithium hexafluorophosphate ($LiPF_6$) was used. It is important to highlight the role of the imaging electron on the reaction: when high energy (300 kV in this work) electrons irradiate the solution,

Received: July 21, 2017
Accepted: September 22, 2017
Published: October 3, 2017

DOI: 10.1021/acsomega.7b01046
ACS Omega 2017, 2, 6329−6336

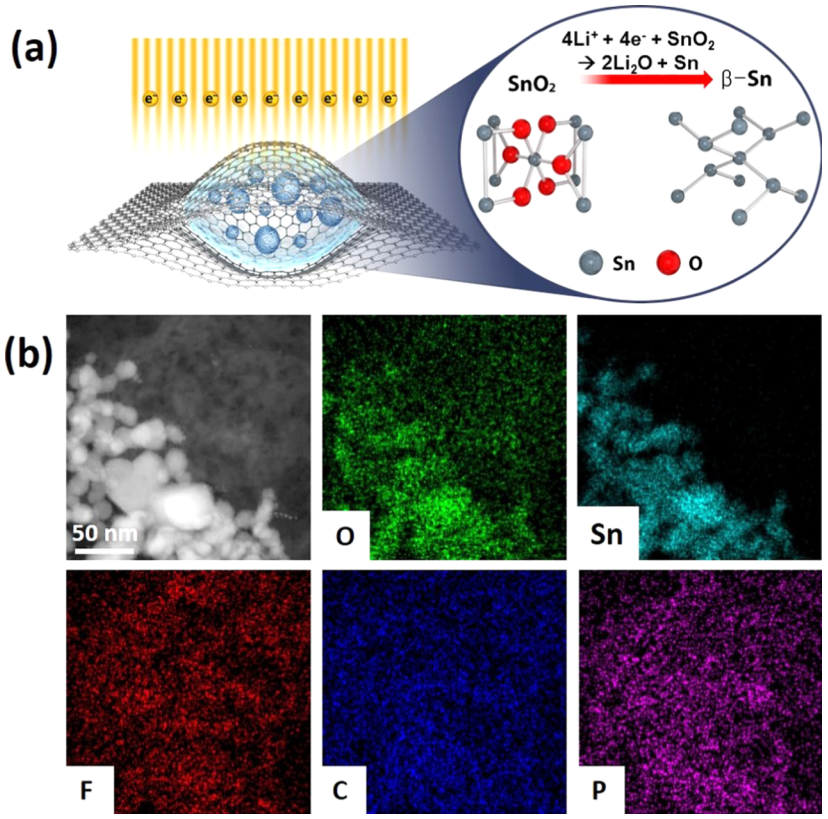

Figure 1. (a) Schematic illustration of the in situ TEM observation of GLC containing SnO_2 NPs undergoing the conversion reaction. They are encapsulated in the organic electrolytes with 1.3 M of $LiPF_6$. (b) Annular dark field scanning transmission electron microscopy (ADF-STEM) images of SnO_2 NPs and transmission electron microscopy energy dispersive X-ray spectroscopy (TEM-EDS) mapping of O, Sn, F, C, and P.

both primary and secondary scattering take place.[20] In the case of the complex organic electrolyte system, the radicals and solvated electrons generated from different scatterings interact with Li salt and electrolyte through a secondary chemical reaction.[20] As a result, upon e-beam irradiation, electrons are supplied from the e-beam and $LiPF_6$ is decomposed into LiF and PF_5 in the electrolyte,[19,20] where LiF can further decompose to produce Li^+ by e-beam irradiation.[19,21] As the graphene synthesized from chemical vapor deposition (CVD) has no defects or functional groups on the surface, it is suggested that its inert surface has minimal chemical and physical interactions with encapsulated electrolyte or NPs. In addition, using graphene sheets minimizes charging and heating effects under the electron beam, as they have excellent electrical and thermal conductivity.[22] GLC is stable upon e-beam irradiation both at 200 and 300 kV,[18,19,23] which shows that in situ TEM observation using GLC can be conducted for a considerable duration of time. Additionally, it was suggested from previous work[18] that enough liquid can be encapsulated inside the graphene sheets (larger than 500 nm in diameter), so enough liquid electrolyte can be present inside the graphene sheets to trigger lithiation. As a result, in situ TEM observation of lithiation behavior was successfully observed by using GLC, as shown in the illustration (Figure 1a) and in previous works.[18,19]

Annular dark field scanning transmission electron microscopy (ADF-STEM) images and transmission electron microscopy energy dispersive X-ray spectroscopy (TEM-EDS) mapping of as-encapsulated SnO_2 NPs inside the GLC are shown in Figure 1b, where SnO_2 NPs are distributed inside the GLC. Energy electron loss spectroscopy (EELS) mapping of Li, which are dispersed in the electrolytes between the graphene sheets, was also characterized (Figure S1). Each element was located in the suitable position, where O, F, C, P, and Li were present in different parts, but Sn was selectively present in the part where SnO_2 NPs were present. SnO_2 NPs had various sizes (10−25 nm) and shapes, and the crystal structure of SnO_2 was the cassiterite structure, confirmed by the selected area diffraction (SAED) pattern, high-resolution transmission electron microscopy (HRTEM) images, and X-ray diffraction (XRD) pattern (Figure S2), showing the well-defined polycrystalline structure.

General processes in the conversion dynamics of SnO_2 NPs take place inside the GLC, which are shown in Figure 2. In the initial stage of lithiation (Figure 2a), it can be seen that some Sn NPs were nucleated from the surface of SnO_2, as Li reacts with SnO_2 to form Sn, according to the chemical reaction ($4Li^+ + 4e^- + SnO_2 \rightarrow 2Li_2O + Sn$). To initially confirm whether those NPs that were initially formed on the surface of SnO_2 were Sn, we conducted another in situ TEM observation by GLC and took the HRTEM image in the boundary of SnO_2 and the nucleated NPs (Figure S3). As evidenced by the HRTEM image, the small NPs were Sn, which were on the surface of SnO_2. Sn NPs were selected from snapshots of the real-time movie, and they were clearly distinguishable because their size (initially, 2−3 nm) was much smaller than that of SnO_2 NPs (~20 nm). It is interesting to note that as-formed Sn NPs were all moving along the surface of SnO_2 NPs, without using the pathway in the electrolyte and within the vacant sites inside the SnO_2 NPs. It is suggested that the motion of weakly bounded NPs inside the liquid is the main driving force for such motion, as shown in the previous in situ TEM work using

DOI: 10.1021/acsomega.7b01046
ACS Omega 2017, 2, 6329−6336

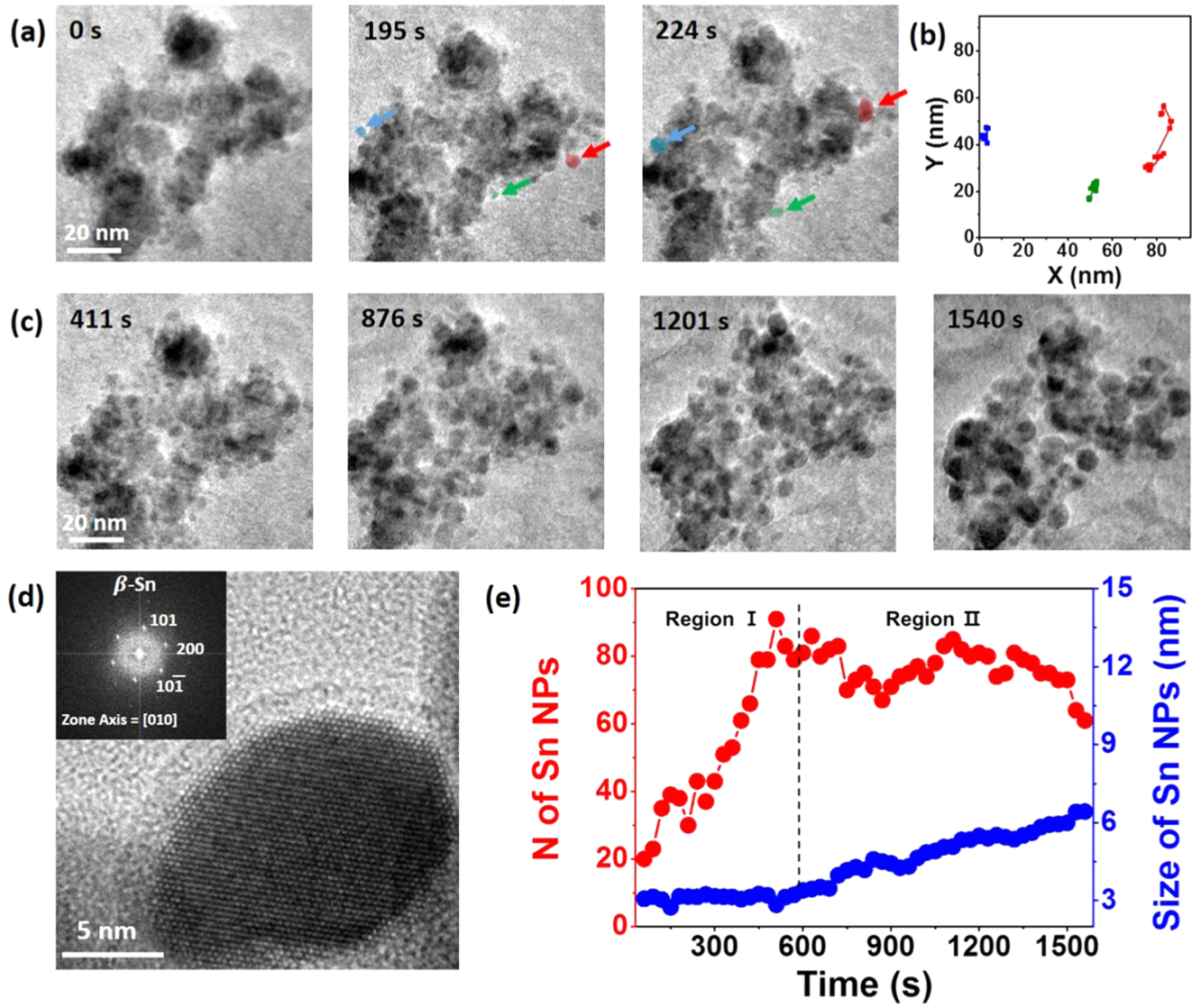

Figure 2. (a) Time-series TEM images of SnO_2 NPs undergoing the conversion reaction, where Sn NPs move along the amorphous shell to be attached to another Sn NP along the surface. (b) Trajectories of red, green, and blue particle motion in the solution based on the movie. (c) Time-series TEM images showing the nucleation and growth of Sn NPs, with increase in the size of Sn NPs with respect to the observation time. (d) HRTEM image of Sn NPs embedded in the amorphous region (inset: fast Fourier transform (FFT) pattern of Sn NP), confirming β-Sn NP structure. (e) The number (red) and average size (blue) of Sn NPs during the in situ observation in (a) and (c) vs time.

liquid solution.[24,25] The weakly bound NPs show different movement compared to that of freely moving NPs inside the liquid. Such difference comes from NPs' movement that is weakly bound to the surface of the window membrane or other nearby particles, where the movement of those NPs is significantly limited. In our case, because Sn NPs do not freely move inside the liquid but move along the surface of SnO_2 NPs, this can be considered as the motion of weakly bounded NPs. The two-dimensional diffusion coefficient (D) was calculated as 0.47 $nm^2\ s^{-1}$ from the equation $D = \langle x^2 \rangle / 4t$, where $\langle x^2 \rangle$ represents the mean-square displacement and t represents the time. The calculated value (0.47 $nm^2\ s^{-1}$) was not much different from the value (0.165−0.268 $nm\ s^{-1}$) measured in the previous literature, with Au NPs of 5−15 nm, as indicated from the study.[25]

To visualize the motion of Sn NPs, two-dimensional trajectories of three Sn NPs in GLC (indicated as red, blue, and green) are shown (Figure 2b). Considering time-series images and trajectories, it can be summarized that Sn NPs generated from the conversion reaction randomly move along the surface of SnO_2 NPs and merge when they are in contact with one another.

In addition, the amorphous shell was formed on the surface of SnO_2 NPs (Figure S4a,b), which is confirmed as Li_xO (Figure S4c), as the EELS spectrum of both Li_2O and Li_2O_2 had similar peaks (Figure S5). Previously, it has been reported that diffusion of Li takes place in an amorphous Li_xO matrix,[26] as there are enough defects for Li ions to pass through. Additionally, the broad peaks at 61−62 and 65−69 eV in Figure S4c suggest that LiF was also formed along with Li_xO, indicating the formation of a solid electrolyte interphase (SEI) layer.[18] Upon the formation of the SEI layer, Li ions can also penetrate and react with SnO_2, where the conversion reaction continues to take place. As lithiation proceeds, the amorphous shell is formed into a denser and uniformly distributed layer, as shown at 416 s (Figure S4a). Although it was previously reported that such an intermediate interface was presumed to be that of Sn, Li, and O,[26] we were able to identify the chemical

DOI: 10.1021/acsomega.7b01046
ACS Omega 2017, 2, 6329−6336

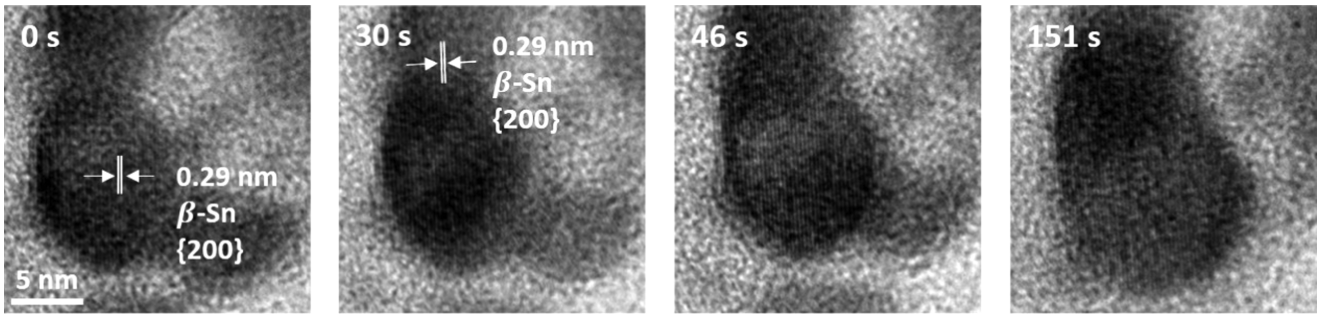

Figure 3. Time-series HRTEM images showing the process of coalescence of two Sn NPs. Initially, rotation of planes is visible. As time proceeds, through necking and merging of individual NPs, two Sn NPs eventually coalesce into one Sn NP.

composition of the layer through EELS analysis. It was confirmed from the EELS spectrum that the chemical composition of the amorphous layer was Li_xO, which is in agreement with the previous literature.[26] To examine the origin of Li_xO, the Li salt was dissolved in the electrolyte upon e-beam irradiation and both high-angle annular dark field scanning transmission electron microscopy (HAADF-STEM) images and the EELS spectrum were taken (Figure S6). In contrast to the EELS spectrum in Figure S4c, the overall peak locations were different (having two peaks at 61 and 69 eV). This is attributed to the formation of LiF as a result of the decomposition of $LiPF_6$ upon e-beam irradiation, in agreement with the previous literature.[18] The results demonstrate that the decomposition product of Li salt is somewhat different from the chemical composition of the amorphous layer, where the amorphous layer was formed as a result of the conversion reaction.

As lithiation proceeds, more Sn NPs are formed in different places and they themselves begin to agglomerate with each other (Figure 2c). At 411 s, more Sn NPs are nucleated, which are mostly fixed in the amorphous matrix. At 876 s, it can be shown that the average size of Sn NPs increased compared with that at 411 s, which suggests that growth of Sn NPs occurred, and as time passes through 1201 and 1540 s, it is seen that even larger Sn NPs are formed, suggesting that agglomeration of Sn NPs has certainly taken place. Along with the agglomeration of Sn NPs, it is also important to note that in the observation time range of 411 to 1201 s, more Sn NPs are still formed as a result of the conversion reaction, where coexistence of Sn NPs and SnO_2 NPs is actually visible in the HRTEM image (Figure S7). Eventually, at 1540 s, almost all of SnO_2 NPs have been converted to Sn NPs, where some Sn NPs are almost connected to each other, which demonstrate that agglomeration of Sn NPs continues throughout the whole process of lithiation. Such agglomerated Sn NPs are mostly embedded within the amorphous matrix, where they have about 5−15 nm diameter with a spherical shape, as shown in Figure 2d. From the HRTEM analysis, it was shown that the crystal structure of precipitated Sn NPs was tetragonal β-Sn (confirmed by the fast Fourier transform (FFT) pattern), which is in good agreement with the previously reported work.[27] The phase transition of SnO_2 NPs from SnO_2 to Sn in the process of lithiation has also been confirmed by time-series SAED patterns (Figure S8), where SnO_2 initially present at 0 s underwent progressive phase transition to β-Sn as time proceeded, leading to complete β-Sn at 1800 s. At 1200 s, both SnO_2 and Sn exist together, which suggests that in the intermediate stage of the conversion reaction, Sn NPs exist as a result of the conversion reaction, whereas some SnO_2 NPs yet remain.

To quantitatively examine how the growth of Sn NPs occurs on a specific time scale, the number and average size of Sn NPs present in the snapshots of the in situ TEM observation shown in Figure 2a,c were calculated every 30 s during observation, from 60 to 1560 s (Figure 2e). On the basis of the calculated data, it can be suggested that different morphological and phase transitions were present with respect to the observation time. From about 60 to 450 s, the nucleation of Sn NPs is predominant, where the number of Sn NPs significantly increases with respect to the observation time, but the average size of Sn NPs barely increases. Then, from about 450 to 1350 s, the nucleation and growth of Sn NPs occur simultaneously, where some Sn NPs are still formed because some remaining SnO_2 NPs undergo the conversion reaction, but at the same time some Sn NPs are attached to other Sn NPs to be merged into larger Sn NPs. Considering the fact that as-formed Sn NPs have diameters between 2 and 3 nm, although some agglomerated Sn NPs may have larger diameters, formation of many new Sn NPs results in continued growth in average diameter of Sn NPs, where more Sn NPs are agglomerated and formed into larger NPs as time proceeds. The number of Sn NPs somewhat decreases and increases from one to another time scale, demonstrating that the formation of new Sn NPs and merging of Sn NPs into larger Sn NPs happen simultaneously.

From 1350 s, almost all SnO_2 NPs underwent the conversion reaction, where only Sn NPs and the amorphous matrix are present. The number of Sn NPs decreases as agglomeration of Sn NPs continues to take place, and the average size of Sn NPs steadily increases with the existence of larger Sn NPs. On the other hand, in contrast to the observation shown from the above time series, in TEM images of SnO_2, the time-series TEM observation of SnO_2 NPs in the electrolytes without $LiPF_6$ showed no distinct morphological evolution (Figure S9). The results suggest that $LiPF_6$ acted as a Li source to trigger lithiation in our case of study, where without $LiPF_6$, there is no source to trigger such a lithiation process. On the basis of the previous works,[18−20] it is suggested that the presence of salt ($LiPF_6$) triggers decomposition of electrolytes, where the decomposition of organic solvents does not necessarily occur without the presence of the salt. Without using $LiPF_6$, such phase evolution and growth of Sn NPs do not occur, which excludes the possibility that it is the organic electrolyte that contributes to the dynamical changes of SnO_2 NPs.

On the basis of the trends in the number of Sn NPs and the average size of Sn NPs, kinetics of the conversion process can further be elucidated (Figure S10). On the basis of the growth of Sn NPs, it can be divided into two different regions (region I and region II). In the first region (marked as region I),

DOI: 10.1021/acsomega.7b01046
ACS Omega 2017, 2, 6329−6336

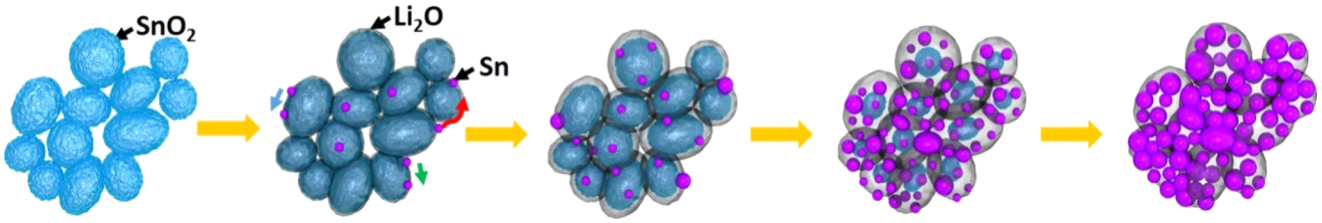

Figure 4. Schematics of the overall conversion and agglomeration process. Upon initial lithiation of SnO_2, a thin amorphous shell was initially formed, with the nucleation of Sn NPs, some of which move along the surface to be attached to other Sn NPs. As lithiation proceeds, more Sn NPs are formed and they subsequently undergo coalescence to be merged into larger Sn NPs, which are positioned in the amorphous matrix.

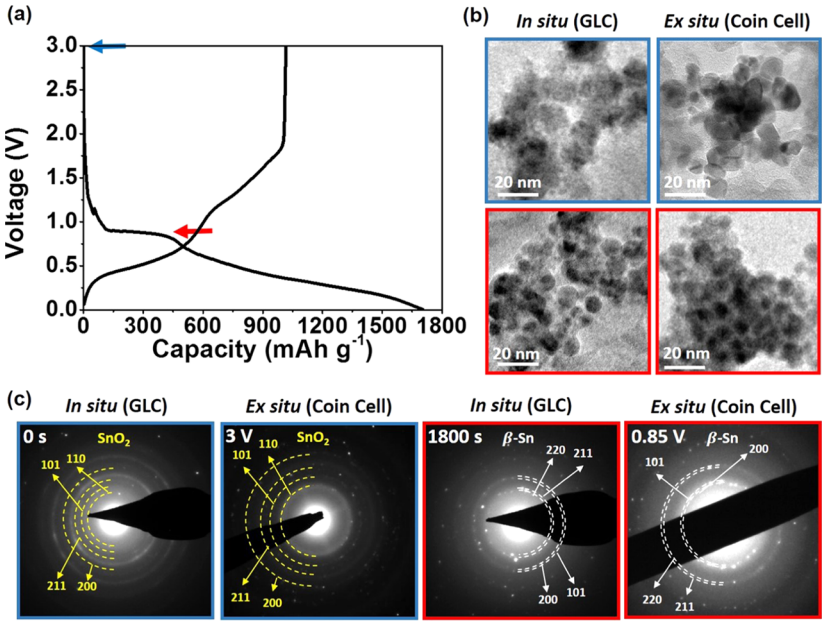

Figure 5. (a) Charge and discharge profile of the SnO_2 NPs under electrochemical lithiation and (b) comparison of in situ and ex situ TEM images of SnO_2 NPs before lithiation (blue box) and after the conversion reaction (red box). (c) Comparison of SAED patterns of SnO_2 NPs under GLC and the electrochemical system before lithiation (blue) and after the conversion reaction (red box). Both in situ and ex situ TEM images are in good agreement, which suggests that in situ TEM observation using GLC is a reliable way to observe phase transition.

nucleation of NPs is dominant. The size of Sn NPs increases proportionally to $t^{1/30}$ (here, time is denoted as t), which means that very slow increase in the size of Sn NPs takes place. The second region (marked as region II), however, shows a growth-dominant behavior. The size of Sn NPs increases proportionally to $t^{1/2}$, which corresponds to a reaction-limited growth according to the Lifshitz−Slyozov−Wagner theory, as shown in the previous literature.[28] Nevertheless, the number of Sn NPs decreases after 600 s, which also suggests that the overall growth process of Sn NPs during the conversion reaction is a complicated system that starts from nucleation to a reaction-limited growth, in addition to the coalescence of Sn NPs.

HRTEM Analysis on the Coalescence of Sn. Regarding the details on how the coalescence of Sn NPs progresses, time-series HRTEM images were taken to show the different stages for the coalescence of two individual Sn NPs (Figure 3). At 0 s, the upper and bottom NPs were in random contact, where each of them was positioned in a different orientation. Up to 30 s, the upper NPs rotated and both NPs' (200) plane was visible because they were not in same orientation. At 46 s, the neck was formed between two NPs on the (200) plane, which acted as diffusion path for Sn atoms. It is important to note that favorable planes for neck formation are known to occur in planes having the lowest surface energy because for metallic NPs, coalescence of NPs usually happens in the planes of the lowest surface energy.[22,29] For face centered cubic NPs,[22] the lowest surface energy is on {111} planes, so their necking and coalescence proceed on {111} planes. For the β-Sn structure, because it is tetragonal, it has the lowest surface energy on the {100}[30] plane, so neck formation and merging of two NPs occur on {200} plane, and as a result, at 151 s, two NPs were completely merged into one NP. Compared with the recently published work that also observed the coalescence of two NPs,[29] this work has two important advancements in (i) the atomic scale observation of coalescence of NPs upon lithiation and (ii) initial report on the coalescence of tetragonal NPs.

Overall Conversion and Agglomeration Dynamics. The schematic design is illustrated in Figure 4 that depicts the overall conversion and agglomeration dynamics of NPs. Upon e-beam irradiation, the amorphous shell is formed on the surface of SnO_2 NPs, where Sn NPs having few nanometers are formed as a result of the conversion reaction with the amorphous matrix. Some of the Sn NPs that are formed on the surface of SnO_2 NPs then move along the amorphous shell until they reach the location at which a nearby Sn NP is present. Sn NPs are then attached to each other and become one NP. As lithiation proceeds, more Sn NPs are formed and are bonded together, mainly by coalescence. At the end of the

DOI: 10.1021/acsomega.7b01046
ACS Omega 2017, 2, 6329−6336

conversion state, SnO_2 is completely transformed into Sn, where much larger Sn NPs are positioned in the amorphous matrix, as explained in the previous literature.[31] The dominant driving force for the agglomeration of Sn NPs was moderate coalescence, but additional driving forces, such as monomer attachment and Ostwald ripening, were also occasionally present (Figure S11), similar to what was reported in the previous work.[32] For instance, the individual monomer (atom or few atoms) moves (820 s) and is attached to nearby NPs (1040 s), resulting in the growth of Sn NPs. In addition, Ostwald ripening takes place: small NPs disappear and a large NP grows, where small NP once present at 798 s is absent at 1227 s. To sum up, the usual occurrence of Sn NP coalescence along with the occasional occurrence of monomer attachment and Ostwald ripening contributed to the agglomeration of Sn NPs.

Comparative Ex Situ Analysis and Evaluation of Study. It is important to highlight that in situ TEM observations shown in this study are similar to the actual reaction products of SnO_2 NPs under the electrochemical reaction. One of the possible drawbacks of GLC is the unrealistic observation caused by lithiation from e-beam rather than the applied bias, although both ways can allow the charge transport to undergo the dynamical changes upon lithiation. In addition, there are other possible limitations in utilizing GLC for in situ TEM observation, as there are no counter electrodes. To confirm whether the in situ TEM observation using GLC is in good agreement with the actual observation in electrochemical cells, in situ TEM images were compared with ex situ TEM images of coin cells that were tested under electrochemical conditions (Figure 5). Electrochemical testing was conducted for SnO_2 as the electrode for LIBs in 2032 coin-type half cells containing Li metal as the reference electrode. The formation cycle was run, which is the initial step of electrochemical testing. Charge and discharge profiles of SnO_2 NPs are shown in Figure 5a, where it shows that the plateau region is at 0.85 V. The presence of the plateau means that the two-phase reactions are taking place at a designated voltage, where reduction of SnO_2 to Sn takes place, in agreement with the previous literature.[31,33] From this understanding, for the ex situ TEM analysis, the cell undergoing the electrochemical test was stopped at 0.85 V and the electrode containing SnO_2 NPs was taken from the cell. Examinations of both in situ and ex situ TEM images before the lithiation (blue box) and after the conversion reaction (red box) were used for comparison of the GLC and coin cell (Figure 5b), where they were in good agreement. Before lithiation, both in situ and ex situ TEM images showed multiple SnO_2 NPs, which were connected to each other. After the conversion reaction (red box), both in situ and ex situ TEM images showed a number of Sn NPs, where the general morphology of Sn NPs shown in in situ TEM images is very similar to that in ex situ TEM images.

Furthermore, SAED patterns (Figure 5c) of SnO_2 NPs both before lithiation and after the conversion reaction in the GLC and coin cell with electrochemical testing have confirmed the presence of SnO_2 (cassiterite) and Sn (β-Sn), respectively. Additionally, to confirm whether the reaction pathways of SnO_2, as shown in this in situ TEM observation, are similar to those under the real electrochemical reaction, we have conducted the ex situ TEM analysis (Figure S12) of electrodes before lithiation, at 0.9 V (in the middle of the conversion reaction) and 0.85 V (last stage of the conversion reaction). Similar to what was observed in the in situ TEM observation, the reaction proceeded from the formation of Sn NPs and the overall conversion of SnO_2 to Sn as the electrochemical reaction took place. This demonstrates that the observation we have taken through TEM by using GLC is in good agreement with actual electrochemical reaction products. To investigate the conversion reaction at each stage, along with ex situ TEM analysis, Raman spectroscopy was conducted at the initial stage, intermediate stage (0.9 V), and end stage (0.85 V) (Figure S13). At first, the E_g, A_{1g}, and B_{1g} peaks[34] at 467, 630, and 772 cm^{-1} were clearly visible but slowly decreased as the conversion reaction proceeded. This is due to the disappearance of the Sn−O bond, which is direct evidence that SnO_2 is transformed to metallic Sn (the peak that is related to the surface defect),[35,36] confirming that the phase transition is in agreement with in situ TEM analysis. The results suggest that reliable in situ TEM observation of electrode materials upon lithiation can be possible by using GLC, as realistic electrolyte conditions can be viable in the GLC system.

CONCLUSIONS

In summary, we have realized the in situ TEM observation of the complete conversion reaction and agglomeration dynamics of NPs inside liquid electrolyte. Sn NPs are nucleated from the surface of the SnO_2 NPs and randomly move around to merge with other Sn NPs. Coalescence is one of the main driving forces in a simultaneous manner that results in the agglomeration and enlargement of Sn NPs. The coalescence mechanism for Sn NPs is a stepwise process of (i) rotation to (200) planes, (ii) formation of necks, and (iii) subsequent merging. Comparative analyses of both in situ and ex situ TEM images and SAED patterns suggest the new opportunities for fully utilizing GLC to observe complete conversion dynamics and agglomeration dynamics of NPs in realistic condition. This work will likely benefit the development of efficient rechargeable batteries using metal oxide NPs with higher capacity and cycling stability, as the fundamental insights regarding the phase transitions and morphological evolution can be gained for not only advanced metal oxide NPs (such as composite with metal oxide NPs, metal/metal oxide alloy NPs, and metal oxide NPs coated with various surficial layers) but also other high-capacity anode NPs (such as Si and Ge) on the basis of in situ TEM observation, which lead to optimized electrode designs for superior electrochemical performance.

EXPERIMENTAL SECTION

Materials and GLC Preparation. SnO_2 NPs were purchased from Sigma-Aldrich (nanopowder <100 nm particle size). The average diameters of the particles were 10−25 nm. The electrolyte used in this study was 1.3 M $LiPF_6$ dissolved in a solvent mixture of EC/DEC (v/v = 3:7) with 10 wt % of fluoroethylene carbonate (FEC). Before the preparation of GLC, 0.006 g of SnO_2 NPs were dispersed in 3 g of liquid electrolyte and the solution was sonicated for 3 h. GLC was prepared by the following procedures. First, multilayer graphene was synthesized by chemical vapor deposition (CVD), using a Cu foil (99.8%, Alfa Aesar) as the substrate. To remove impurities and oxides on the surface, the Cu foil was etched with 20% phosphoric acid (HF, 85%, Junsei) for 20 min. After placing the Cu foil in the CVD chamber, the temperature was set to 1050 °C for 30 min and stabilized for 60 min with 200 standard cubic centimeters per minute (sccm) of H_2 gas. Then, as the carbon source, 20 sccm of CH_4 gas was added for

DOI: 10.1021/acsomega.7b01046
ACS Omega 2017, 2, 6329−6336

25 min and the synthesis was ended by cooling the chamber to room temperature, at a rapid rate. With this procedure, 2−15 layers of multilayer graphene were synthesized. It is reported that multilayer graphene can increase the yield of liquid cells, while having little effect of resolution in TEM observation, compared with monolayer graphene. Next, the synthesized multilayer graphene was transferred to the holey carbon Au TEM grid (quantifoil, 300 mesh, hole size = 2 μm) by the direct transfer method.[37] Using 0.2 M ammonium persulfate ($(NH_4)_2S_2O_8$, Sigma-Aldrich) solution for 6 h, Cu foil was etched and no longer visible. The reason that Au TEM grids were used is that during this etching step, Cu TEM grids are likely be dissolved with Cu foil during the etching step. With two graphene-transferred grids, the graphene liquid cell was prepared by dropping 20 μL of electrolyte containing SnO_2 NPs, $LiPF_6$, and EC/DEC (v/v = 3:7), with 10 wt % of FEC on one graphene-transferred grid, and putting the other graphene-transferred grid onto the top. Finally, the liquid drop was dried and encapsulated by van der Waals forces between two graphene sheets.

TEM Analysis. A JEOL JEM-3010 TEM and charge coupled device camera (SC200, Gatan) were used for in situ observation under 300 kV accelerating voltage. EDS elemental mapping was obtained using JEOL JEM ARM200F under 200 kV accelerating voltage. EELS mapping and spectrum were obtained by using GIF Quantum 966 in the Titan ETEM G^2 microscope at 80 and 300 kV condition, respectively.

Cell Assembly and Electrochemical Cell Testing. Ex situ TEM images were taken on the electrode that was composed of SnO_2 NPs, super P carbon black, and poly(acrylic acid)/sodium carboxymethyl cellulose (50/50 wt %, Aldrich) binder at a weight ratio of 80:10:10, as reported similarly in the previous works.[18] They were mixed together with deionized water and deposited on Cu current collector by slurry casting and dried in a vacuum oven for 150 °C for 2 h. The loading amount of active material was about 2 mg cm^{-2}. It was assembled into the 2032 coin-type half cells, which consisted of lithium metal as a counter electrode, separator (Celgard 2325), and an electrolyte consisting of 1.3 M $LiPF_6$ in EC/DEC (3/7 v/v) with 10 wt % of FEC, which is an identical electrolyte used for GLC. It was cycled at a current density of 50 mA g^{-1} between 0.01 and 3 V, using a battery testing device (WBCS4000, Wonatech). During the discharge process, cycling was stopped at about 0.85 V and the electrode was taken out from the half cell. It was washed with dimethyl carbonate and dried for 10 min in the glovebox and analyzed with TEM.

■ ASSOCIATED CONTENT

Supporting Information

The Supporting Information is available free of charge on the ACS Publications website at DOI: 10.1021/acsomega.7b01046.

EELS mapping of Li; TEM image, SAED pattern, and XRD pattern of SnO_2 NPs; snapshot TEM images of formation of the amorphous shell on the surface of SnO_2 NPs, HRTEM image of the amorphous shell, and the EELS spectrum of Li_xO; EELS spectrum of Li_2O_2 and Li_2O; HAADF-STEM image and EELS signal of GLC in low magnification; HRTEM image showing the coexistence of SnO_2 and Sn NPs; in situ SAED patterns of SnO_2 in GLC with respect to the observation time; time-series TEM images of SnO_2 NPs in the electrolyte without $LiPF_6$; linear approximation on the growth rate of Sn NPs; TEM images of two additional driving forces for the nucleation and growth of Sn NPs; ex situ TEM images of SnO_2 NPs in the electrochemical reaction; ex situ Raman spectrum of SnO_2 NPs in the electrochemical reaction (PDF)

Formation of amorphous shell on the surface of SnO_2 NPs (AVI)

Conversion dynamics of SnO_2 NPs under lithiation (AVI)

Coalescence dynamics of Sn NPs under high resolution (AVI)

SnO_2 NPs in the electrolyte containing no $LiPF_6$ (AVI)

■ AUTHOR INFORMATION

Corresponding Authors

*E-mail: idkim@kaist.ac.kr (I.-D.K.).
*E-mail: j.y.lee@kaist.ac.kr (J.Y.L.).

ORCID

Joon Ha Chang: 0000-0001-8877-9917
Jong Min Yuk: 0000-0002-4677-7363
Sung Joo Kim: 0000-0001-9776-1532
Il-Doo Kim: 0000-0002-9970-2218

Author Contributions

§J.H.C. and J.Y.C. contributed equally to this work.

Author Contributions

The manuscript was written through contributions of all authors. J.H.C. and J.Y.C. contributed equally to this work. J.M.Y., I.-D.K., and J.Y.L. led the direction of research. J.Y.C. and C.K. assembled the cells and conducted electrochemical cell tests. J.H.C. fabricated graphene liquid cells. J.H.C., S.J.K., and H.K.S. conducted TEM analysis. J.Y.C. characterized the electrode materials. J.H.C. and J.Y.C. wrote the manuscript. All authors reviewed the manuscript.

Notes

The authors declare no competing financial interest.

■ ACKNOWLEDGMENTS

This work was supported by the Korea CCS R&D Center (KCRC) grant funded by the Korean government (Ministry of Science, ICT & Future Planning) (No. NRF-2014M1A8A1049303), End-Run grant from KAIST funded by the Korean government in 2016 (Ministry of Science, ICT & Future Planning) (N11160058), NRF (National Research Foundation of Korea) Grant funded by the Korean Government (NRF-2017H1A2A1042006-Global Ph.D. Fellowship Program), Wearable Platform Materials Technology Center (WMC) (NR-2016R1A5A1009926), Nano·Material Technology Development Program through the National Research Foundation of Korea (NRF) funded by the Ministry of Science, ICT and Future Planning (2009-0082580), National Research Foundation of Korea (NRF) grant funded by the Korean government (MSIP; Ministry of Science, ICT & Future Planning) (NRF-2017R1C1B5017962), and Institute for Basic Science (IBS) (IBS-R004-D1).

■ REFERENCES

(1) Xu, J.; Ding, W.; Zhao, W.; Zhao, W.; Hong, Z.; Huang, F. In Situ Growth Enabling Ideal Graphene Encapsulation upon Mesocrystalline $MTiO_3$ (M = Ni, Co, Fe) Nanorods for Stable Lithium Storage. *ACS Energy Lett.* **2017**, *2*, 659−663.

DOI: 10.1021/acsomega.7b01046
ACS Omega 2017, 2, 6329−6336

(2) Li, H.; Balaya, P.; Maier, J. Li-Storage via Heterogeneous Reaction in Selected Binary Metal Fluorides and Oxides. *J. Electrochem. Soc.* **2004**, *151*, A1878−A1885.
(3) Zhou, X.; Wan, L.-J.; Guo, Y.-G. Synthesis of MoS_2 nanosheet-graphene nanosheet hybrid materials for stable lithium storage. *Chem. Commun.* **2013**, *49*, 1838−1840.
(4) Reddy, M. V.; Subba Rao, G. V.; Chowdari, B. V. R. Metal Oxides and Oxysalts as Anode Materials for Li Ion Batteries. *Chem. Rev.* **2013**, *113*, 5364−5457.
(5) Oh, H.-J.; Jo, C.-H.; Yoon, C. S.; Yashiro, H.; Kim, S.-J.; Passerini, S.; Sun, Y.-K.; Myung, S.-T. Nickel oxalate dihydrate nanorods attached to reduced graphene oxide sheets as a high-capacity anode for rechargeable lithium batteries. *NPG Asia Mater.* **2016**, *8*, No. e270.
(6) Ponrouch, A.; Taberna, P.-L.; Simon, P.; Palacin, M. R. On the origin of the extra capacity at low potential in materials for Li batteries reacting through conversion reaction. *Electrochim. Acta* **2012**, *61*, 13−18.
(7) Lee, S.-Y.; Park, K.-Y.; Kim, W.-S.; Yoon, S.; Hong, S.-H.; Kang, K.; Kim, M. Unveiling origin of additional capacity of SnO_2 anode in lithium-ion batteries by realistic *ex situ* TEM analysis. *Nano Energy* **2016**, *19*, 234−245.
(8) Xiao, L.; Wang, S.; Wang, Y.; Meng, W.; Deng, B.; Qu, D.; Xie, Z.; Liu, J. High-Capacity and Self-Stabilized Manganese Carbonate Microspheres as Anode Material for Lithium-Ion Batteries. *ACS Appl. Mater. Interfaces* **2016**, *8*, 25369−25378.
(9) Liu, B.; Jin, L.; Zheng, H.; Yao, H.; Wu, Y.; Lopes, A.; He, J. Ultrafine Co-based Nanoparticle@Mesoporous Carbon Nanospheres toward High-Performance Supercapacitors. *ACS Appl. Mater. Interfaces* **2017**, *9*, 1746−1758.
(10) He, C.; Wu, S.; Zhao, N.; Shi, C.; Liu, E.; Li, J. Carbon-Encapsulated Fe_3O_4 Nanoparticles as a High-Rate Lithium Ion Battery Anode Material. *ACS Nano* **2013**, *7*, 4459−4469.
(11) Zhu, C.; Mu, X.; van Aken, P. A.; Yu, Y.; Maier, J. Single-Layered Ultrasmall Nanoplates of MoS_2 Embedded in Carbon Nanofibers with Excellent Electrochemical Performance for Lithium and Sodium Storage. *Angew. Chem., Int. Ed.* **2014**, *53*, 2152−2156.
(12) Bhaway, S. M.; Chen, Y.-M.; Guo, Y.; Tangvijitsakul, P.; Soucek, M. D.; Cakmak, M.; Zhu, Y.; Vogt, B. D. Hierarchical Electrospun and Cooperatively Assembled Nanoporous Ni/NiO/MnO_x/Carbon Nanofiber Composites for Lithium Ion Battery Anodes. *ACS Appl. Mater. Interfaces* **2016**, *8*, 19484−19493.
(13) Xu, L.; Hu, Y.; Zhang, H.; Jiang, H.; Li, C. Confined Synthesis of FeS_2 Nanoparticles Encapsulated in Carbon Nanotube Hybrids for Ultrastable Lithium-Ion Batteries. *ACS Sustainable Chem. Eng.* **2016**, *4*, 4251−4255.
(14) Qi, K.; Wei, J.; Sun, M.; Huang, Q.; Li, X.; Xu, Z.; Wang, W.; Bai, X. Real-time Observation of Deep Lithiation of Tungsten Oxide Nanowires by In Situ Electron Microscopy. *Angew. Chem., Int. Ed.* **2015**, *54*, 15222−15225.
(15) Su, Q.; Xie, J.; Zhang, J.; Zhong, Y.; Du, G.; Xu, B. In Situ Transmission Electron Microscopy Observation of Electrochemical Behavior of CoS_2 in Lithium-Ion Battery. *ACS Appl. Mater. Interfaces* **2014**, *6*, 3016−3022.
(16) Hwang, S.; Lee, Y.; Jo, E.; Chung, K. Y.; Choi, W.; Kim, S. M.; Chang, W. Investigation of Thermal Stability of P2-Na_xCoO_2 Cathode Materials for Sodium Ion Batteries Using Real-Time Electron Microscopy. *ACS Appl. Mater. Interfaces* **2017**, *9*, 18883−18888.
(17) Xia, W.; Zhang, Q.; Xu, F.; Sun, L. New Insights into Electrochemical Lithiation/Delithiation Mechanism of α-MoO_3 by in Situ Transmission Electron Microscopy. *ACS Appl. Mater. Interfaces* **2016**, *8*, 9170−9177.
(18) Cheong, J. Y.; Chang, J. H.; Seo, H. K.; Yuk, J. M.; Shin, J. W.; Lee, J. Y.; Kim, I.-D. Growth dynamics of solid electrolyte interphase layer on SnO2 nanotubes realized by graphene liquid cell electron microscopy. *Nano Energy* **2016**, *25*, 154−160.
(19) Yuk, J. M.; Seo, H. K.; Choi, J. W.; Lee, J. Y. Anisotropic Lithiation Onset in Silicon Nanoparticle Anode Revealed by in Situ Graphene Liquid Cell Electron Microscopy. *ACS Nano* **2014**, *8*, 7478−7485.
(20) Abellan, P.; Mehdi, B. L.; Parent, L. R.; Gu, M.; Park, C.; Xu, W.; Zhang, Y.; Arslan, I.; Zhang, J.-G.; Wang, C.-M.; et al. Probing the Degradation Mechanisms in Electrolyte Solutions for Li-Ion Batteries by in Situ Transmission Electron Microscopy. *Nano Lett.* **2014**, *14*, 1293−1299.
(21) Ghatak, J.; Guan, W.; Mobus, G. In situ TEM observation of lithium nanoparticle growth and morphological cycling. *Nanoscale* **2012**, *4*, 1754−1759.
(22) Yuk, J. M.; Park, J.; Ercius, P.; Kim, K.; Hellebusch, D. J.; Crommie, M. F.; Lee, J. Y.; Zettl, A.; Alivisatos, A. P. High-Resolution EM of Colloidal Nanocrystal Growth Using Graphene Liquid Cells. *Science* **2012**, *336*, 61−64.
(23) Lee, K.; Shin, S.; Degen, T.; Lee, W.; Yoon, Y. S. In situ analysis of SnO2/Fe2O3/RGO to unravel the structural collapse mechanism and enhanced electrical conductivity for lithium-ion batteries. *Nano Energy* **2017**, *32*, 397−407.
(24) Chee, S. W.; Baraissov, Z.; Loh, N. D.; Matsudaira, P. T.; Mirsaidov, U. Desorption-Mediated Motion of Nanoparticles at the Liquid-Solid Interface. *J. Phys. Chem. C* **2016**, *120*, 20462−20470.
(25) Zheng, H.; Claridge, S. A.; Minor, A. M.; Alivisatos, A. P.; Dahmen, U. Nanocrystal Diffusion in a Liquid Thin Film Observed by in Situ Transmission Electron Microscopy. *Nano Lett.* **2009**, *9*, 2460−2465.
(26) Wang, C.-M.; Xu, W.; Liu, J.; Zhang, J.-G.; Saraf, L. V.; Arey, B. W.; Choi, D.; Yang, Z.-G.; Xiao, J.; Thevuthasan, S.; et al. In Situ Transmission Electron Microscopy Observation of Microstructure and Phase Evolution in a SnO2 Nanowire during Lithium Intercalation. *Nano Lett.* **2011**, *11*, 1874−1880.
(27) Huang, J. Y.; Zhong, L.; Wang, C. M.; Sullivan, J. P.; Xu, W.; Zhang, L. Q.; Mao, S. X.; Hudak, N. S.; Liu, X. H.; Subramanian, A.; et al. In situ observation of the electrochemical lithiation of a single SnO2 nanowire electrode. *Science* **2010**, *330*, 1515−1520.
(28) Woehl, T. J.; Evans, J. E.; Arslan, I.; Ristenpart, W. D.; Browning, N. D. Direct in Situ Determination of the Mechanisms Controlling Nanoparticle Nucleation and Growth. *ACS Nano* **2012**, *6*, 8599−8610.
(29) Wu, F.; Yao, N. In-situ synthesis and defect evolution of single-crystal piezoelectric nanoparticles. *Nano Energy* **2016**, *28*, 195−205.
(30) Sellers, M. S.; Schultz, A. J.; Basaran, C.; Kofke, D. A. Atomistic modeling of β-Sn surface energies and adatom diffusivity. *Appl. Surf. Sci.* **2010**, *256*, 4402−4407.
(31) Liang, J.; Yu, X.-Y.; Zhou, H.; Wu, H. B.; Ding, S.; Lou, X. W. D. Bowl-like SnO2@Carbon Hollow Particles as an Advanced Anode Material for Lithium-Ion Batteries. *Angew. Chem., Int. Ed.* **2014**, *53*, 12803−12807.
(32) Jeong, M.; Yuk, J. M.; Lee, J. Y. Observation of Surface Atoms during Platinum Nanocrystal Growth by Monomer Attachment. *Chem. Mater.* **2015**, *27*, 3200−3202.
(33) Cheong, J. Y.; Kim, C.; Jang, J. S.; Kim, I.-D. Rational design of Sn-based multicomponent anodes for high performance lithium-ion batteries: SnO2@TiO2@reduced graphene oxide nanotubes. *RSC Adv.* **2016**, *6*, 2920−2925.
(34) Zhao, Q.; Ju, D.; Deng, X.; Huang, J.; Cao, B.; Xu, X. Morphology-modulation of SnO_2 Hierarchical Architectures by Zn Doping for Glycol Gas Sensing and Photocatalytic Applications. *Sci. Rep.* **2015**, *5*, No. 7874.
(35) Kim, W. J.; Lee, S. W.; Sohn, Y. Metallic Sn spheres and SnO_2@C core-shells by anaerobic and aerobic catalytic ethanol and CO oxidation reactions over SnO_2 nanoparticles. *Sci. Rep.* **2015**, *5*, No. 13448.
(36) Sinha, A. K.; Sil, A.; Sasmal, A. K.; Prahan, M.; Pal, T. Synthesis of active tin: an efficient reagent for allylation reaction of carbonyl compounds. *New J. Chem.* **2015**, *39*, 1685−1690.
(37) Yuk, J. M.; Zhou, Q.; Chang, J.; Ercius, P.; Alivisatos, A. P.; Zettl, A. Real-Time Observation of Water-Soluble Mineral Precipitation in Aqueous Solution by In Situ High-Resolution Electron Microscopy. *ACS Nano* **2016**, *10*, 88−92.

DOI: 10.1021/acsomega.7b01046
ACS Omega 2017, 2, 6329−6336